Planar channel flow of a discontinuous shear-thickening model fluid: theory and simulation

A. Vázquez-Quesada,[1, a)] N. J. Wagner,[2, b)] and M. Ellero[1, c)]

[1)] *Zienkiewicz Centre for Computational Engineering (ZCCE), Swansea University, Bay Campus, Swansea SA1 8EN, United Kingdom.*

[2)] *Department of Chemical and Biomolecular Engineering, University of Delaware, 150 Academy Street, Colburn Laboratory, Newark, DE 19716, USA*

In this work an analytical solution for the pressure-driven flow of a discontinuous shear-thickening (DST) fluid in a planar channel is presented. In order to model the fluid rheology, a regularized inverse-biviscous model is adopted. This involves a region of finite thickness to model the sharp jump in viscosity and it is consistent with momentum conservation. In the limit of vanishing thickness, the truly DST behavior is obtained. Analytical results are validated by numerical simulations under steady and start-up flow using the Smoothed Particle Hydrodynamics method. Flow results are investigated and discussed for different values of the model parameters.

[a)] Electronic mail: A.Vazquez-Quesada@swansea.ac.uk

[b)] Electronic mail: wagnernj@udel.edu

[c)] Electronic mail: M.Ellero@swansea.ac.uk

I. INTRODUCTION

Shear-thickening (ST) is a typical phenomenon encountered in many particle dispersions which refers to a significant increase of suspension viscosity when large shear-rates or stresses are applied[1]. It happens typically at very large shear rates and has profound implications. ST represents a challenging problem for several processing conditions as it limits transport of paints, inks and other concentrated dispersions in spraying, coating and pumping operations but, when properly controlled, can be also used to engineer novel materials as selective dampers and shock absorbers[2,3]. The physics behind the onset of shear-thickening, have been traditionally proposed based on several mechanisms ranging from dilatancy[4], flow-induced expansion of the suspension or irreversible shear-induced aggregation related to stable flocculated states[5], to order-disordered transitions[6,7].

Reversible shear-thickening has been also reported in colloidal systems which differs from early study of dilatancy, where the increased viscosity is associated to the appearance of so-called hydroclusters[8–12], and dominance of short-range interparticle lubrication forces[8–10]. The idea is that upon increasing shear rate, convective forces dominate over entropic repulsive Brownian forces, being able to bring particles close together forming transient hydrodynamic aggregates. In the thin gaps between particles inside hydroclusters, diverging lubrication forces are active which in turn induce large stresses in the system. The existence of hydroclusters was confirmed by experiments[12–14] flow-small angle neutron scattering[13–15], optical methods including flow dichroism[13,16], fast confocal microscopy[12] and numerical simulations[8–10].

The previous hydrodynamic thickening scenario corresponds to a significant -still continuous- increase of the suspension viscosity upon increasing shear rate and it is therefore generally denoted as "continuous shear thickening" (CST) in the literature. Although recent simulations have suggested that a large increase in suspension viscosity can be obtained considering only interparticle lubrication forces in connection with particle deformability -i.e. elastohydrodynamic lubrication[17] - or with external confinement[18] - it is now generally acknowledged that the sudden jump (as opposite to continuous mild rise) in the viscosity observed in some systems, i.e. the so called "discontinuous shear thickening" (DST), might be of non-hydrodynamic nature. The microscopic origin of DST has been explained in terms of, for example, flow-induced dynamic-jamming theories[19], as well as impact-activated

solidification[20]. In particular, the addition of surface frictional forces[21–23], rather than purely hydrodynamic interactions acting between particles, has been proposed to capture the observed liquid/solid-like transition observed in the DST of very concentrated suspensions. In fact, the presence of surface roughness, friction, and finite particle inertia can all lead to a shear-rate dependent microstructure and rheology[24–26]. Shear-thickening has been also reported in particle suspensions interacting with viscoelastic matrices[27], but the nature behind that ST behavior seems to be related to the non-Newtonian properties of the matrix, i.e. strain hardening of the polymers in highly extensional regions - rather than direct interparticle forces, such as lubrication in Newtonian suspending media or frictional contact in granular systems.

Although much work has been done towards the understanding of the microscopic origin of the continuous and discontinuous shear-thickening transition, modelling and simulation of the macroscopic behavior of a DST fluid has been limited. In particular, some theoretical analysis at the continuum level - i.e. on spatial scales much larger than the colloidal particle size - have been made using generalized Newtonian power-law models, Carreau Yasuda models or quadratic models with selective choice of the power exponents[26,28–33]. It should be pointed out, however, that in all these studies the flow of a mild "continuous" shear thickening fluid has been considered. To the best of our knowledge no simulation has been presented for a truly DST fluid[1,34,35] and, more specifically, no mathematical analysis of its flow behavior has been made so far. In particular, the numerically validated analytical solution for the planar channel flow of a DST fluid as proposed in this work, represents an essential requirement to construct new lubrication models[36] for particles interacting in a DST matrix, a system which is receiving increasingly attention in experiments[35].

In this work, we try to remedy to the lack of macroscopic modelling of DST fluids by analyzing theoretically and performing simulations of a DST fluid flowing in a confined geometry, i.e. a classical pressure-driven planar channel flow. A model for a DST fluid based on an "inverse" bi-viscous scheme is proposed. The standard bi-viscous model describes a fluid characterized by two viscous regimes, a low-shear-rate/high-viscous regime followed by a low-viscous regime at high shear rates. By choosing the critical shear rate for the viscous transition sufficiently small, it has been applied in the past as a model of plastic fluids characterized by an apparent yield stress. We explore here the behavior of

the *inverse* bi-viscous model (inverse small-to-high viscous transition) as a simplified description of a DST transition and study its steady and transient flow behavior in a planar channel geometry. Simulations of the DST fluid using the so called Smoothed Particle Hydrodynamic (SPH) method[37–39] - which has been already successfully applied to different non-Newtonian/viscoelastic flows[40–42]- have been also performed to validate the analytical results.

The scheme of the paper is the following. In Sec. I, the geometry and the inverse bi-viscous models are described in detail. Sec. II is devoted to the analytical derivation of the steady solution for this model fluid. In Sec. III we present the SPH methods used for the numerical simulation and we validate numerically the analytical results of Sec. II. Finally, in Sec. IV we report the conclusion and we highlight the implications as well as the limitations of the present results.

II. PLANAR CHANNEL FLOW OF A DST FLUID: ANALYTICAL SOLUTION

In this section we describe the model adopted for the DST fluid as well as the geometrical setup and regime of flow. A discontinuous shear-thickening fluid is modelled here as a so-called "inverse" bi-viscous fluid with the viscosity defined as

$$\eta = \begin{cases} \eta_0, & \text{if } \dot{\gamma} \leq \dot{\gamma}_c - \delta\dot{\gamma} \\ m\dot{\gamma} + n, & \text{if } \dot{\gamma}_c - \delta\dot{\gamma} < \dot{\gamma} \leq \dot{\gamma}_c + \delta\dot{\gamma} \\ \eta_1, & \text{if } \dot{\gamma} > \dot{\gamma}_c + \delta\dot{\gamma} \end{cases} \tag{1}$$

where $\dot{\gamma}$ is the local shear rate, $\dot{\gamma}_c$ is the critical shear rate corresponding to the viscous transition and $\delta\dot{\gamma}$ determines the width of shear rates where the viscosity changes from η_0 to η_1. In contrast to the standard bi-viscous model, $\eta_1 > \eta_0$ is considered. The liquid/solid-like transition observed in DST fluids at high shear rates is modelled here by a linear liquid-liquid transition between two regimes characterized by a large viscosity ratio occurring over a small finite range of shear rates with thickness $\Delta = \delta\dot{\gamma}/\dot{\gamma}_c \ll 1$ (see Fig. 1). For $\delta\dot{\gamma} \to 0$ the singular discontinuous model is obtained (red line). The linear transition is necessary to regularize the model and remove the discontinuity of the viscosity function at the critical shear rate $\dot{\gamma}_c$ which would lead to stress discontinuity and non-conservation of momentum.

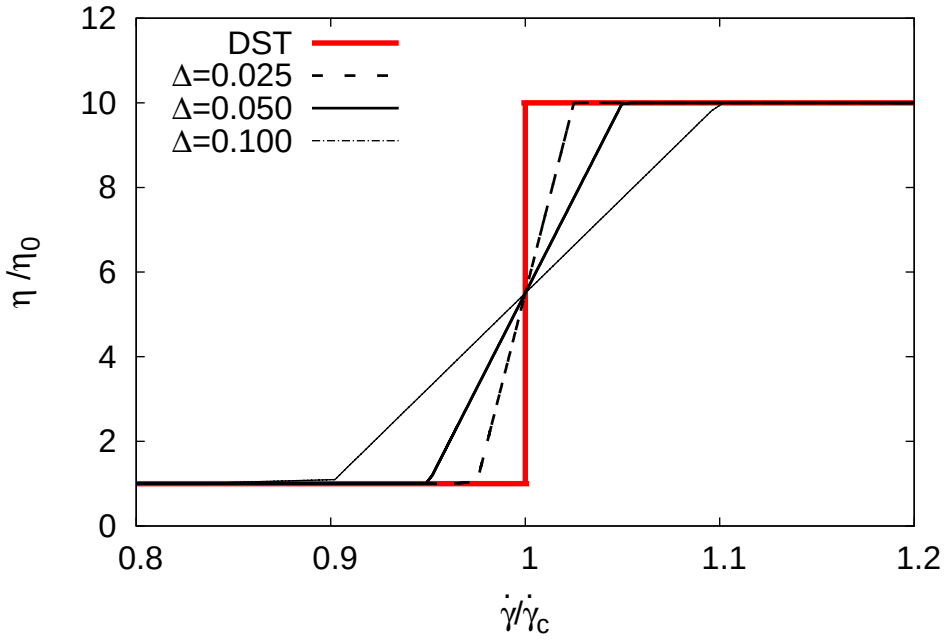

FIG. 1. Viscosity vs normalized shear rate: shear thickening model with a "smooth" transition with thickness $\Delta = \delta\dot{\gamma}/\dot{\gamma}_c \ll 1$ for the case $\eta_1/\eta_0 = 10$. The limiting behavior for $\Delta \to 0$ (red line) corresponds to a discontinuous shear thickening model.

The specific values of the coefficients m and n ensuring the continuity of the viscosity are

$$m = \frac{\eta_1 - \eta_0}{2\delta\dot{\gamma}}$$
$$n = \frac{1}{2\delta\dot{\gamma}} \left(\eta_0 \left(\dot{\gamma}_c + \delta\dot{\gamma}\right) - \eta_1 \left(\dot{\gamma}_c - \delta\dot{\gamma}\right)\right). \tag{2}$$

Note also that in experiments with particle suspensions, jumps in the relative viscosity can be in the order of $\mathcal{O}(100)$ or even larger at very high concentrations.

The DST fluid is confined between two planar walls placed at distance L_z apart and it is driven by a constant pressure gradient $\partial p/\partial r$. We denote here z as the direction perpendicular to the walls and r the direction of the flow. As in the standard Poiseuille solution, the flow is assumed periodic in the r direction, whereas spatial dependency of the velocity profile is present in the z direction only. The flow is unidirectional with the only non-vanishing component of the velocity field being of the type $u_r = u(z)$. Before to work out the exact solution in the following sections, we discuss qualitatively first the flow regimes expected for such a configuration.

A trivial situation is obtained in the case when the local shear rates $\dot{\gamma} = \partial u(z)/\partial z \leq \dot{\gamma}_c - \delta\dot{\gamma}$ at every position z across the channel, i.e. the maximum actual shear rate is not

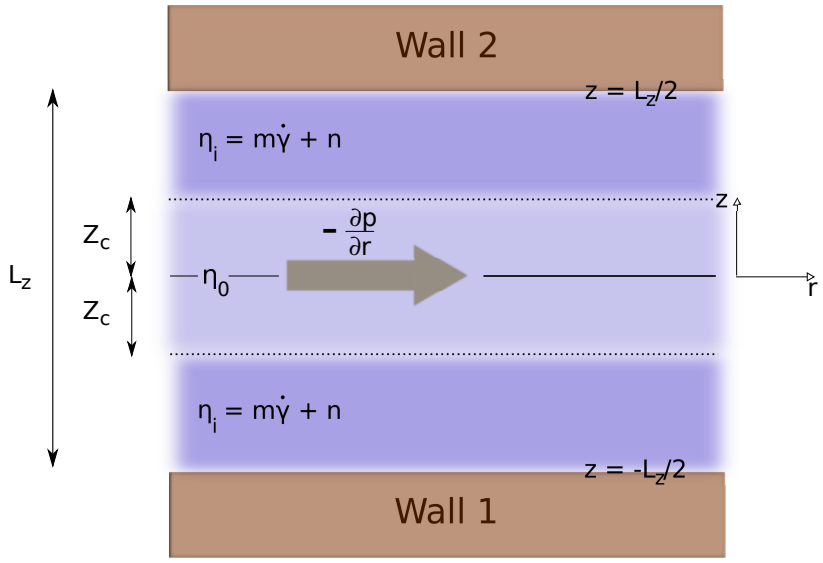

FIG. 2. Scheme of the problem in the regime II case (intermediate pressure gradient).

high enough to trigger the viscous transition in the fluid. In this case (regime I), typically occurring at small pressure gradients, the fluid behaves as a simple Newtonian fluid, with constant viscosity η_0, and the corresponding steady-state solution is given by the classical Poiseuille formula.

If the gradient of pressure is increased, a region will eventually appear where the fluid does not behave as Newtonian, i.e. for z such that $\dot{\gamma} > \dot{\gamma}_c - \delta\dot{\gamma}$ a transition to higher viscosity η_1 will take place. As the shear rate is greatest at the wall $\dot{\gamma}_w$, the previous condition translates to

$$\dot{\gamma}_w = \left|\frac{\partial u(z)}{\partial z}\right|_{z=Lz/2} = \frac{L_z}{2\eta_0}\frac{\partial p}{\partial r} > \dot{\gamma}_c - \delta\dot{\gamma} \Longrightarrow \frac{\partial p}{\partial r} > \frac{2\eta_0\left(\dot{\gamma}_c - \delta\dot{\gamma}\right)}{L_z}, \tag{3}$$

which characterizes the onset of regime II (intermediate pressure gradient).

As depicted in Fig. 2., for the intermediate pressure gradient regime defined by Eq. (3), two regions can be distinguished, one with low viscosity η_0 at $|z - c| < z_c$ (close to the middle plane where the shear rate must be zero for symmetry reasons) and another (near-wall layer where the shear rate is maximum) corresponding to a viscosity $\eta_0 < \eta \leq \eta_1$.

If the gradient pressure is increased further, the liquid-liquid transition layer of viscosity $\eta_0 < \eta \leq \eta_1$ will enlarge towards the middle plane. If the shear rate in the wall exceeds the value $\dot{\gamma}_c + \delta\gamma$ another layer of viscosity η_1 close to the wall will appear. That happens when

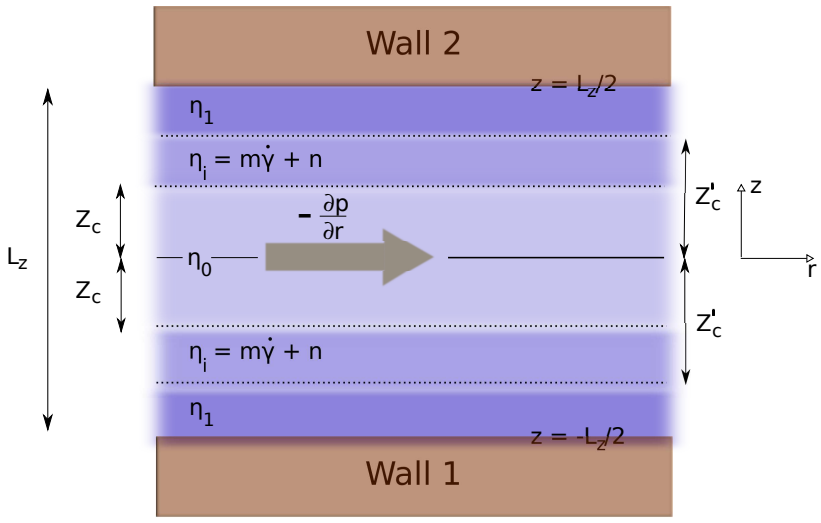

FIG. 3. Scheme of the problem in the regime III case (high pressure gradient).

the next condition on the pressure gradient is held

$$\frac{\partial p}{\partial r} > \frac{2\eta_1\left(\dot{\gamma}_c + \delta\dot{\gamma}\right)}{L_z}, \tag{4}$$

which characterizes the onset of regime III (high pressure gradient) (see Fig. 3) .

In the next subsections an exact analytical solution of the velocity profile and flow rate of this problem will be calculated and their limit in the DST case (when $\delta\dot{\gamma} \to 0$) discussed.

A. Velocity profile calculation

If the origin is located at the center of the gap, in order to conserve the linear momentum, the shear rate is related with the pressure gradient as follows

$$\eta(\dot{\gamma})\dot{\gamma} = \left|\frac{\partial p}{\partial r} z\right|. \tag{5}$$

The values of z_c and z_c' (distances from the center to the coordinate where the shear rate equals to $\dot{\gamma}_c - \delta\dot{\gamma}$ and $\dot{\gamma}_c + \delta\dot{\gamma}$ respectively) can be calculated from Eq. (5) as

$$z_c = \frac{\eta_0\left(\dot{\gamma}_c - \delta\dot{\gamma}\right)}{|\partial p/\partial r|}, \quad z_c' = \frac{\eta_1\left(\dot{\gamma}_c + \delta\dot{\gamma}\right)}{|\partial p/\partial r|}. \tag{6}$$

The different regimes considered previously can be defined in terms of the latter distances. If $z_c \geq L_z/2$ the system is in the regime I. The regime II shows up when $z_c < L_z/2$ and $z_c' \geq L_z/2$. Finally, the regime III should be considered if $z_c' < L_z/2$.

When Eq. (5) is applied to the different viscosity zones, the shear rate of those regions can be calculated, obtaining

$$\begin{aligned}
\dot{\gamma}_0(z) &= \frac{1}{\eta_0}\left|\frac{\partial p}{\partial r} z\right|, \quad \text{if } |z| \leq z_c \\
\dot{\gamma}_i(z) &= -\phi\left(1+\sqrt{1+\frac{2}{n\phi}\left|z\partial p/\partial r\right|}\right), \quad \text{if } z_c < |z| \leq z_c' \\
\dot{\gamma}_1(z) &= \frac{1}{\eta_1}\left|\frac{\partial p}{\partial r} z\right|, \quad \text{if } |z| > z_c'
\end{aligned} \tag{7}$$

where the sub-indices 0, i and 1 have been used to refer to the quantities in the regions indicated in the equation. These sub-indices will be used consistently in this work. In the above equation the next function has also been defined: $\phi = n/(2m)$. The chosen solution for $\dot{\gamma}_i$ is the only one holding that $\dot{\gamma}_i > 0$. It has also been considered that $n < 0$, assumption which is valid as long as

$$\delta\dot{\gamma} < \dot{\gamma}_c\left(\frac{\eta_1 - \eta_0}{\eta_1 + \eta_0}\right). \tag{8}$$

From the shear rate, the derivative $\partial u(z)/\partial z$ can be obtained. It reads

$$\begin{aligned}
\frac{\partial u_0(z)}{\partial z} &= \frac{1}{\eta_0}\frac{\partial p}{\partial r} z \\
\frac{\partial u_i(z)}{\partial z} &= -s\phi\left(1+\sqrt{1+\frac{2s}{n\phi} z\partial p/\partial r}\right) \\
\frac{\partial u_1(z)}{\partial z} &= \frac{1}{\eta_1}\frac{\partial p}{\partial r} z
\end{aligned} \tag{9}$$

where $s = \text{sign}\left(z\frac{\partial p}{\partial r}\right)$ and $\phi = n/(2m)$. The velocity profile can be obtained by integration of $\partial u(z)/\partial z$ and considering that the next conditions should be held

$$\begin{aligned}
& & & u_0(\pm L_z/2) = 0, & \text{for regime I} \\
& & u_i(\pm L_z/2) = 0, & \quad u_0(z_c) = u_i(z_c), & \text{for regime II} \\
u_1(\pm L_z/2) = 0, & \quad u_1(z_c') = u_i(z_c'), & \quad u_0(z_c) = u_i(z_c), & \text{for regime III.}
\end{aligned} \tag{10}$$

The analytical velocity profiles read as follows.

For regime I

$$u_0(z) = \frac{1}{2\eta_0}\frac{\partial p}{\partial r}\left(z^2 - \frac{L_z^2}{4}\right). \tag{11}$$

For regime II

$$u_i(z) = f(z) - f(L_z/2)$$
$$u_0(z) = \frac{1}{2\eta_0}\frac{\partial p}{\partial r}\left(z^2 - z_c^2\right) + f(z_c) - f(L_z/2). \tag{12}$$

For regime III

$$u_1(z) = \frac{1}{2\eta_1}\frac{\partial p}{\partial r}\left(z^2 - \frac{L_z^2}{4}\right) \tag{13}$$
$$u_i(z) = f(z) - f(z_c') + \frac{1}{2\eta_1}\frac{\partial p}{\partial r}\left(z_c'^2 - \frac{L_z^2}{4}\right)$$
$$u_0(z) = \frac{1}{2\eta_0}\frac{\partial p}{\partial r}\left(z^2 - z_c^2\right) + \frac{1}{2\eta_1}\frac{\partial p}{\partial r}\left(z_c'^2 - \frac{L_z^2}{4}\right) + f(z_c) - f(z_c')$$

where the function f is defined as

$$f(z) = -\phi\left(\frac{\partial p}{\partial r}\right)^{-1}\left(\left|z\frac{\partial p}{\partial r}\right| + \frac{1}{3}n\phi\left(1 + \frac{2}{n\phi}\left|z\frac{\partial p}{\partial r}\right|\right)^{3/2}\right). \tag{14}$$

B. Flow rate

In order to understand the flow behavior of a DST fluid, it is instructive to analyze its flow rate as a function of the applied pressure gradient. The flow rate can be calculated as

$$Q = \int_{z_1}^{z_2} u(z)dz. \tag{15}$$

Introducing the velocity profiles from the previous section, the obtained flow rate is

$$Q = \begin{cases} Q_I, & \text{for regime I} \\ Q_{II}, & \text{for regime II} \\ Q_{III}, & \text{for regime III} \end{cases} \tag{16}$$

where

$$Q_I = -\frac{1}{12\eta_0}\frac{\partial p}{\partial r}L_z^3$$
$$Q_{II} = 2\left(-\frac{1}{3\eta_0}\frac{\partial p}{\partial r}z_c^3 + z_c f(z_c) - \frac{L_z}{2}f(L_z/2) + g(L_z/2) - g(z_c)\right) \tag{17}$$
$$Q_{III} = 2\left(\frac{1}{3\eta_1}\frac{\partial p}{\partial r}\left(z_c'^3 - \left(\frac{L_z}{2}\right)^3\right) - \frac{1}{3\eta_0}\frac{\partial p}{\partial r}z_c^3 + z_c f(z_c) - z_c' f(z_c') + g(z_c') - g(z_c)\right),$$

being

$$g(z) = -s\phi\left(\frac{1}{2}z^2 + \frac{1}{15}\left(\frac{n\phi}{\partial p/\partial r}\right)^2\left(1 + \frac{2}{n\phi}\left|\frac{\partial p}{\partial r}z\right|\right)^{5/2}\right). \tag{18}$$

C. DST limit

The perfect DST case is obtained in the limit $\delta\dot{\gamma} \to 0$. In this limit the shear rate in the region $z_c < z < z_c'$ reduces to

$$\dot{\gamma}_i = \dot{\gamma}_c. \tag{19}$$

The velocity profiles in the different regimes in such a limit read as follows.
For regime I

$$u_0(z) = \frac{1}{2\eta_0}\frac{\partial p}{\partial r}\left(z^2 - \frac{L_z^2}{4}\right). \tag{20}$$

For regime II

$$\begin{aligned} u_i(z) &= \dot{\gamma}_c\left(|z| - \frac{L_z}{2}\right)\text{sign}\left(\frac{\partial p}{\partial r}\right) \\ u_0(z) &= \frac{1}{2\eta_0}\frac{\partial p}{\partial r}\left(z^2 - z_c\left(L_z - z_c\right)\right). \end{aligned} \tag{21}$$

For regime III

$$\begin{aligned} u_1(z) &= \frac{1}{2\eta_1}\frac{\partial p}{\partial r}\left(z^2 - \frac{L_z^2}{4}\right) \\ u_i(z) &= \dot{\gamma}_c\left(|z| - z_c'\right)\text{sign}\left(\frac{\partial p}{\partial r}\right) + \frac{1}{2\eta_1}\frac{\partial p}{\partial r}\left(z_c'^2 - \frac{L_z^2}{4}\right) \\ u_0(z) &= \frac{1}{2\eta_0}\frac{\partial p}{\partial r}\left(z^2 + z_c^2\right) - \frac{1}{2\eta_1}\frac{\partial p}{\partial r}\left(z_c'^2 + \frac{L_z^2}{4}\right). \end{aligned} \tag{22}$$

Finally, in such a limit the Q_I, Q_{II} and Q_{III} functions for the calculation of the flow rate in the different regimes are given by

$$\begin{aligned} Q_I &= -\frac{1}{12\eta_0}\frac{\partial p}{\partial r}L_z^3 \\ Q_{II} &= -\frac{1}{12\eta_0}\frac{\partial p}{\partial r}z_c\left(3L_z^2 - 4z_c^2\right) \\ Q_{III} &= -\frac{1}{12\eta_0}\frac{\partial p}{\partial r}\left(4z_c\left(z_c'^2 - z_c^2\right) + \frac{\eta_0}{\eta_1}L_z^3\right). \end{aligned} \tag{23}$$

It should be pointed out that, mathematically speaking, this singular limit is not consistent with linearity of the stress profile and momentum conservation. Nevertheless, the velocity profiles and flow rate are approximated very well by the "smooth" DST fluid (Eq.1) for $\delta\dot{\gamma} \to 0$. In Sec. III B we will explore this aspect in detail with simulations.

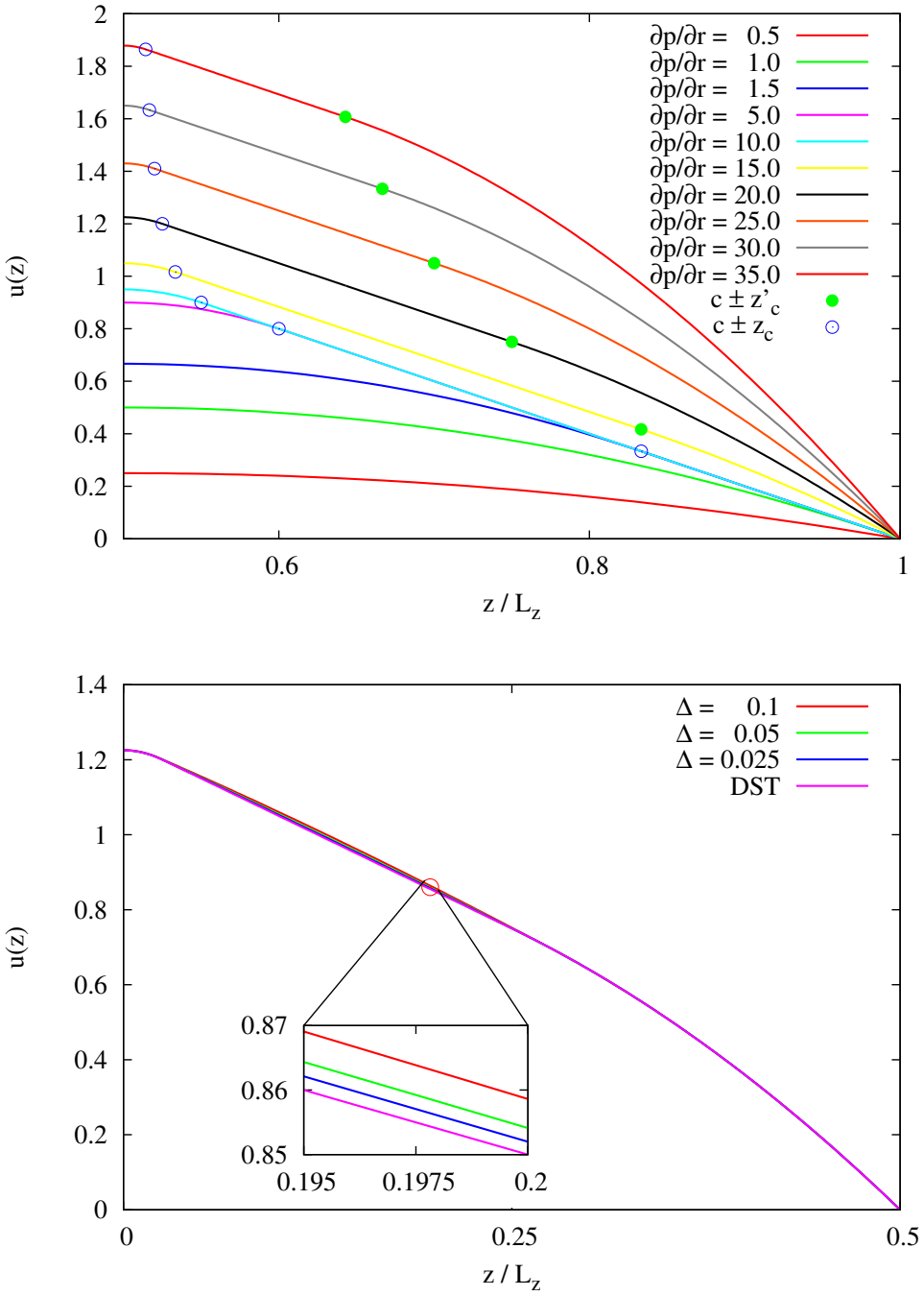

FIG. 4. Velocity profiles for different pressure gradients.

D. Effect of physical parameters on flow behavior

In the Fig. 4 (top) the velocity profiles for different pressure gradients have been drawn for a relative thickness transition corresponding to $\Delta = 0.025$, which is in the quasi-

discontinuous shear-thickening limit. The walls are at $z/L_z = -0.5, 0.5$, but given the symmetry of the profiles, only half a channel has been depicted. The parameters have been taken in such a way that the transition between regimes I and II is given at $\partial p/\partial r = 2\eta_0 \left(\dot{\gamma}_c + \delta\dot{\gamma}\right)/L_z = 1$, whereas the transition pressure gradient between regimes II and III is given at $\partial p/\partial r = 2\eta_1 \left(\dot{\gamma}_c - \delta\dot{\gamma}\right)/L_z = 10$. The viscosity ratio in the inverse bi-viscous model was chosen $\eta_1/\eta_0 = 10$. For sake of clarity, the locations of $\pm z_c$ and $\pm z_c'$ have been drawn with open and filled circles respectively.

From the figure, it can be seen that the velocity profile is parabolic at all z, with viscosity η_0 for small pressure gradients ($\partial p/\partial r = 0.5, 1$). At larger pressure gradients, the parabolic regions shrink towards a vanishing layer centered at the middle plane (see blue circles defining the linear-parabolic transition in the profile). For even larger pressure gradients ($\partial p/\partial r > 10$) a new transition appears (yellow circles), where the near wall-profile returns to parabolic with viscosity η_1. As in the previous case, the intermediate region with viscosity $\eta_0 < \eta < \eta_1$ shrinks to a vanishing middle layer for very large pressure gradients, recovering a complete parabolic profile in the limit $\partial p/\partial r \to \infty$.

To study the effect of Δ on the calculated profiles, in the Fig. 4 (bottom) the velocity profiles for different values of Δ have been drawn for the case $\partial p/\partial r = 20 \times 2\eta_0\dot{\gamma}_c/L_z$. There is a very little difference, with the true DST limit (red line) being well approximated from "smooth" models already for $\Delta = 0.1$. This is more visible from the zoom inset, where the DST solution (orange line) represents the limiting curve towards which the profiles tend by reducing $\delta\dot{\gamma}$. Note that the true DST solution is singular and involves a discontinuity on the stress between the two viscous regions; however, every solution with vanishing (but finite) Δ enforces strictly stress continuity and is consistent with momentum conservation.

The dependence of the flow rate on the pressure gradient is depicted in Fig. 5. At low and high pressure gradients the fluid behaves as a Newtonian with viscosities, respectively, η_0 and η_1. In the intermediate regime, a transition between the two viscous behaviors is observed. Note that within the central regime (II), the flow rate is nearly constant for increasing applied pressure drops, producing an enhancement of flow resistance much larger that the high-viscous regime III. This observation suggests that the physical consequences of using the inverse bi-viscous model are not the result of just joining the effects of two viscous regimes, i.e it exhibits a highly non-linear resistance behavior consistent with a

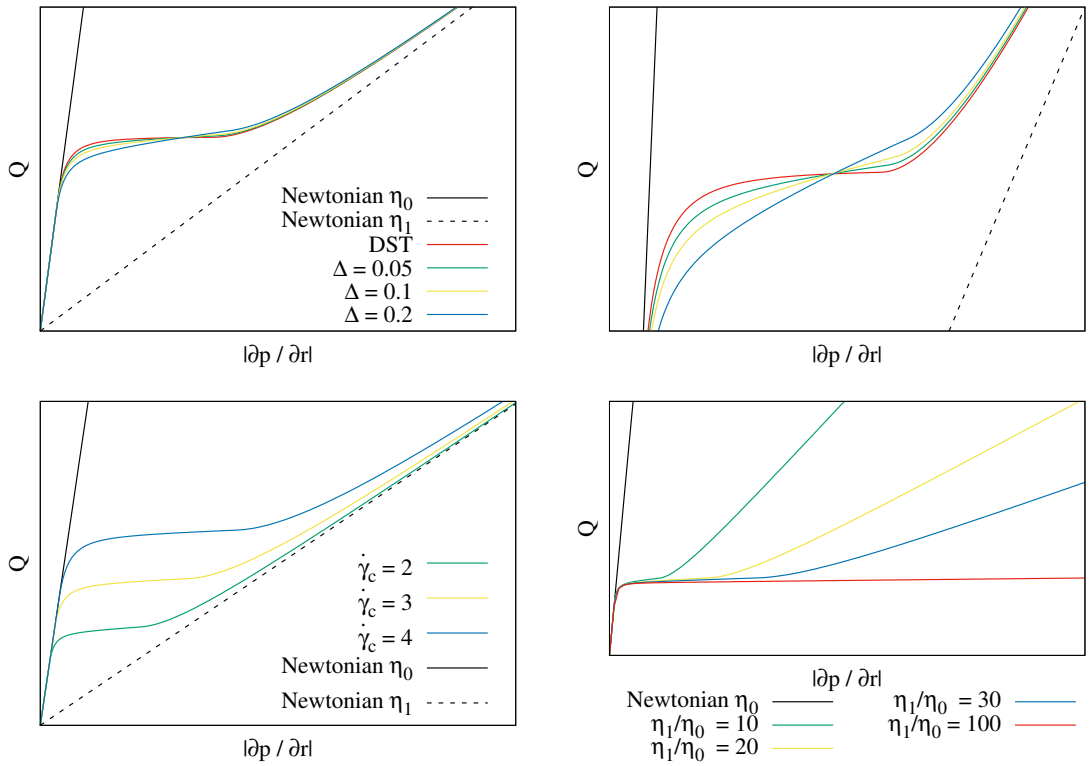

FIG. 5. Flow rate vs pressure gradient. Top left: effect of the thickness Δ (zoom in top right). Bottom left: effect of $\dot{\gamma}_c$. Bottom right: effect of η_1/η_0.

discontinuous shear thickening scenario. Finally, we note that at larger pressure gradients the material returns to flow with a large viscous resistance. This is consistent with recent experiments with dense, non-Brownian suspensions[43] where the stress (up to concentrations 50%) shows two liquid-like power-law regimes at small/high shear-rates matched by a very steep transition in the middle gap (see their Fig. 1).

The effect of the transition thickness Δ is shown in Fig. 5 (top left and top right (zoom)). Note that in the transition region, the singular DST solution corresponds to an exact horizontal line where no flow increase takes place by increasing pressure drop. Solutions at finite thickness approximate that limiting behavior for $\Delta \to 0$. In the same figure, the effect in the model of the parameters $\dot{\gamma}_c$ (bottom left) and the ratio η_1/η_0 (bottom right) are also shown for the case $\Delta = 0.05$. For increasing $\dot{\gamma}_c$ the transitions in regimes I-II and regimes II-III are moved to higher pressure gradients. Increasing η_1 makes the viscosity ratio bigger, leading to an extension of intermediate regime II. In the limit of $\eta_1/\eta_0 \to \infty$ (red line), the regime III can not be reached for any value of the pressure gradient. In the opposite limit,

$\eta_1/\eta_0 \to 1$, the regime II disappears and the flow rate of a Newtonian fluid of viscosity η_0 is recovered.

III. NUMERICAL RESULTS

A. Smoothed Particle Hydrodynamic model of an inverse bi-viscous fluid

The simulation method used in this work to discretize the inverse bi-viscous model is the Smoothed-Particle Hydrodynamics (SPH). SPH is a mesh-free method where the fluid is represented by a set of Lagrangian fluid particles which act as interpolation points for the hydrodynamic fields. To model the bi-viscosity, a modification of the SPH version proposed by Español et al.[37] to simulate the Navier-Stokes equations is used. The new evolutions of the position $\boldsymbol{r}_i$ and velocity $\boldsymbol{v}_i$ of the fluid particle i are given now by

$$\begin{aligned} \frac{d\boldsymbol{r}_i}{dt} &= \boldsymbol{v}_i \\ m\frac{d\boldsymbol{v}_i}{dt} &= -\sum_j \left(\frac{P_i}{\rho_i^2} + \frac{P_j}{\rho_j^2}\right) \cdot \boldsymbol{e}_{ij} W'_{ij} + \sum_j \frac{\eta_i + \eta_j}{\rho_i \rho_j r_{ij}} \boldsymbol{v}_{ij} W'_{ij} \end{aligned} \tag{24}$$

where summations are done over all the particles j in the neighborhood of particle i (i.e. within a distance r_{cut}). m is the fluid particle mass, P_i is the pressure, $\boldsymbol{v}_{ij} = \boldsymbol{v}_i - \boldsymbol{v}_j$ is the difference of velocities, $\boldsymbol{r}_{ij} = \boldsymbol{r}_i - \boldsymbol{r}_j$ the relative position and $\boldsymbol{e}_{ij} = \boldsymbol{r}_{ij}/r_{ij}$ the unit vector along the direction between particles i and j. $W_{ij} = W\left(r = r_{ij}, r_{cut}\right)$ is a compact kernel function (quintic spline) with cutoff radius r_{cut} and its differentiation appearing in Eq. (24) is defined as $W'_{ij} = \partial W\left(r, r_{cut}\right)/\partial r|_{r=r_{ij}}$. The mass density of the particle i is $\rho_i = m d_i$ where the number density is defined as[38]

$$d_i = \sum_j W_{ij}. \tag{25}$$

An equation of state for the pressure is chosen $P_i = c_s^2(\rho_i - \rho_0) + b$, where ρ_0 is the reference mass density and the speed of sound c_s is chosen sufficiently larger than the maximum flow velocity to ensure that the liquid Mach number $\mathrm{Ma} = V_{max}/c_s \ll 1$ and avoid compressible effects. Finally, $\eta_i = \eta(\dot{\gamma}_i)$ where $\dot{\gamma}_i = \|\dot{\boldsymbol{\gamma}}_i\| = (1/2)(\dot{\boldsymbol{\gamma}}_i : \dot{\boldsymbol{\gamma}}_i)^{1/2}$ and the local particle shear rate tensor $\dot{\boldsymbol{\gamma}}$ is estimated as[41]

$$\dot{\boldsymbol{\gamma}}_i = -\frac{1}{d_i} \sum_j W'_{ij} \boldsymbol{e}_{ij} \boldsymbol{v}_{ij}. \tag{26}$$

The inverse bi-viscous model Eq. (1) is used to calculate the local particle viscosity.

B. Steady and transient planar channel flow of a DST fluid: SPH results

The two-dimensional planar geometry is simulated by placing two walls at distance $L_z = 4$ apart. Size of the simulation box in the streaming direction is $L_r = 2.5$. To model solid walls, the Morris boundary conditions[39,40] are adopted to enforce no-slip velocity at the surfaces, whereas classical periodic boundary conditions are used in the streaming direction (r). A constant pressure gradient is applied as an effective body acceleration at time $t = 0$ and the evolution of the velocity profiles are monitored until a steady state is reached. Speed of sound is chosen $c_s = 100$. In the bi-viscous model the low viscosity is $\eta_0 = 24.5833$, high viscosity is $\eta_1 = 10\eta_0$ and $\dot{\gamma}_c = 2$. Based on these parameters, the maximum Mach number ($\mathrm{Ma} = V_{max}/c_s$) and Reynolds number ($\mathrm{Re} = \rho L_z V_{max}/\eta_1$) are both significantly smaller than unity for all flow configurations studied, such that laminar flow is anticipated. Numerical resolutions up to $N_z = 80$ fluid particles spanning the channel gap have been considered. Cutoff radius used in the simulation correspond to $r_{cut} = 3\Delta z$, with $\Delta z = L_z/N_z$ the mean particle spacing. Initially a regular lattice configurations is used.

In the Fig. 6 (top left) the converged steady velocity profile at one applied pressure gradient ($\partial p/\partial r = 300$) is shown and compared with the analytical solution for several values of the transition thickness Δ. As mentioned in the section II D, the velocity profile is only slightly affected by Δ in the range considered. One can better appreciate the differences in the Fig. 6 (top right) where a zoom in the area of biggest deviations is depicted. The SPH results (black lines) fit very well the analytical solution (blue lines) at the corresponding Δ. In particular for $\Delta = 0.05, 0.025$ no deviation is visible even in the zoomed area. Profiles tend towards the truly DST solution (red line).

In order to check the accuracy of the computed solutions, in Fig. 6 (bottom left) the SPH local velocity gradients (black) are compared against theory (blue) and limiting DST solution (red line). For a true DST fluid, a constant $\dot{\gamma} = \dot{\gamma}_c$ is observed in the transitional regime which is the singular limit of the SPH solutions at finite Δ. Accuracy between theory and simulation is excellent. Finally, in Fig. 6 (bottom right) we show the off diagonal component of the stress across the channel. The typical linear symmetric continuous stress profile is obtained in simulations, which is consistent with momentum conservation.

After looking at the effect of Δ on the flow quantities, in Fig. 7 the transient start up flow of the fluid (quasi-DST limit: $\Delta = 0.025$) is shown for four prototypical flow regimes,

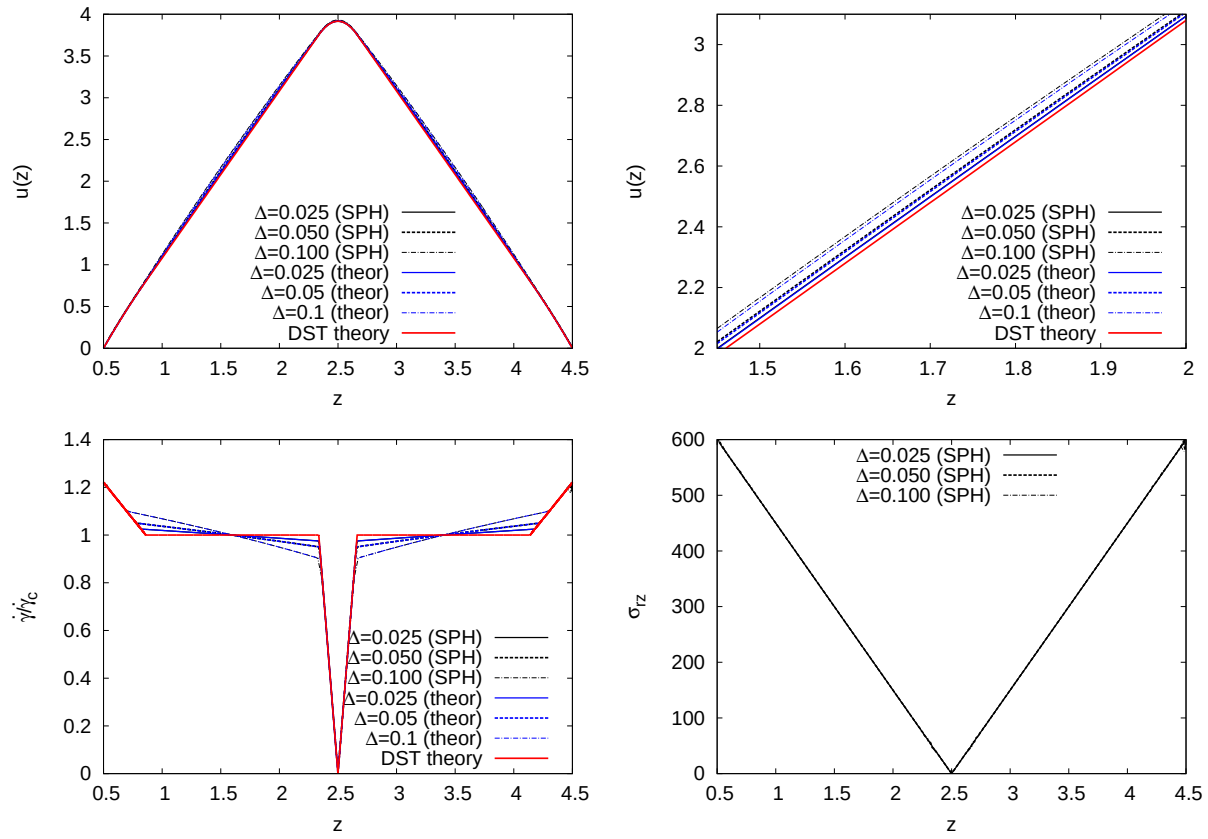

FIG. 6. Top figures: velocity profile at $\partial p/\partial r = 300$ for $\Delta = 0.025, 0.05, 0.1$. Differences are better visible in the zoom plot (top right), where good agreement between theory and SPH is achieved at the corresponding Δ. Bottom left plot: velocity gradient. Bottom-right plot: stress. Red lines correspond to the limiting truly DST solution.

i.e. regime I (top left: low pressure gradient), regime II (top right: intermediate pressure gradient) and regime III (bottom left/right: high pressure gradient). To check the accuracy of the simulations, results corresponding to two numerical resolutions have been depicted, namely $N_z = 40, 80$ fluid particles across the channel gap, indicating that the results are insensitive to change in resolution.

Flow regime I (Fig. 7, top left) shows the typical development of a parabolic profile corresponding to a fluid of constant viscosity η_0. Remaining plots are less trivial and show the effect of the viscous transition on the transient and finally developed velocity profiles. In the flow regime II (Fig. 7, top right) condition (3) is met and the velocity profile develops a transition towards a quasi-linear stretch at almost-constant shear rate $\dot{\gamma}_c$. Initially, the quasi-linear part of the velocity profile is located only near the wall where, due to the large

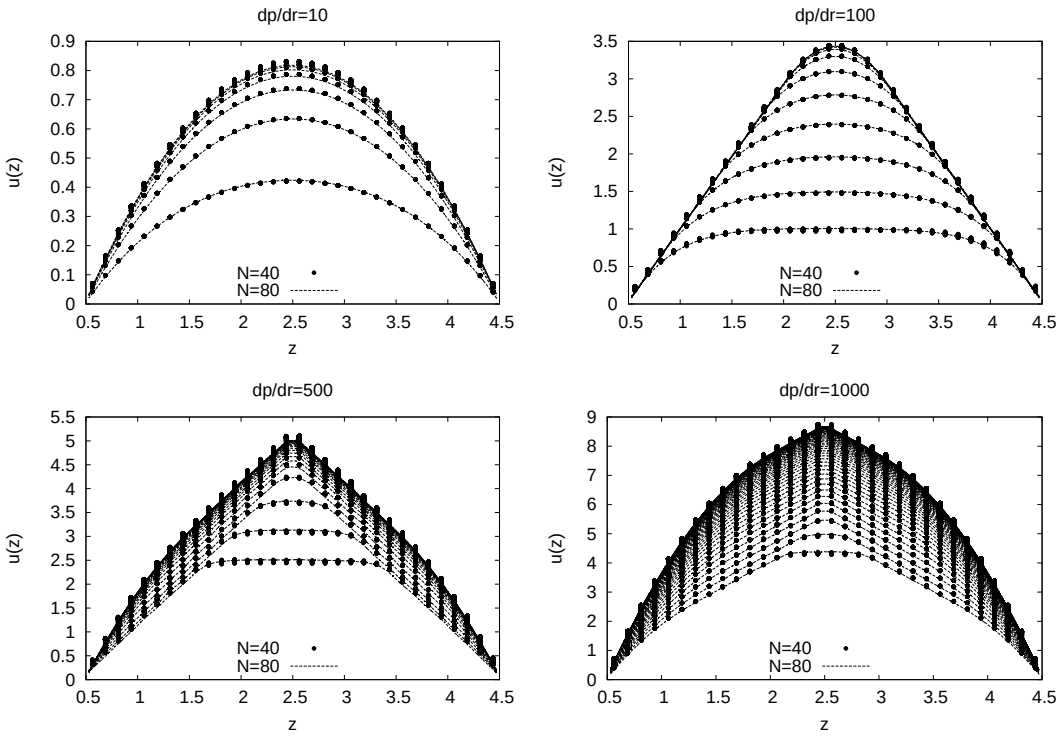

FIG. 7. Start-up flow of an inverse bi-viscous fluid for different applied pressure gradients. Profiles correspond to frames taken at dimensionless time intervals $\Delta T^* = \Delta T/\tau_{\eta_1} = 0.77, 0.077, 0.0192, 0.0096$ respectively for $(\partial p/\partial r = 10, 100, 500, 1000)$. Here, $\tau_{\eta_1} = H^2\rho/\eta_1$ is a viscous reference time.

gradients during start up, the local shear rate exceeds $\dot{\gamma}_c - \delta\gamma_c$. As the flow develops, the quasi-linear velocity profile region stretches towards the middle of the plane according to the corresponding steady-state solution. Note that two flow regions are present under this condition, i.e. near-wall quasi-linear velocity profile and central parabolic velocity profile.

In the bottom plots of Fig. 7 the high-pressure gradient case is shown (regime III). When condition (4) is met, the flow resistance caused by a limiting quasi-linear velocity profile becomes too large, the fluid cannot sustain the stress and an additional high-viscous parabolic region near the wall appears. This is clear from the bottom-left figure where three regimes are present, i.e. parabolic-quasi-linear-parabolic. As in the previous case, the high-viscous parabolic profile is initially located only near the wall, eventually extending towards the middle plane as the flow develops. In the limiting case of very large pressure gradients, the high viscous parabolic profile will pervade quasi the entire space, leaving only a small central layer behaving as in regime II (bottom right plot).

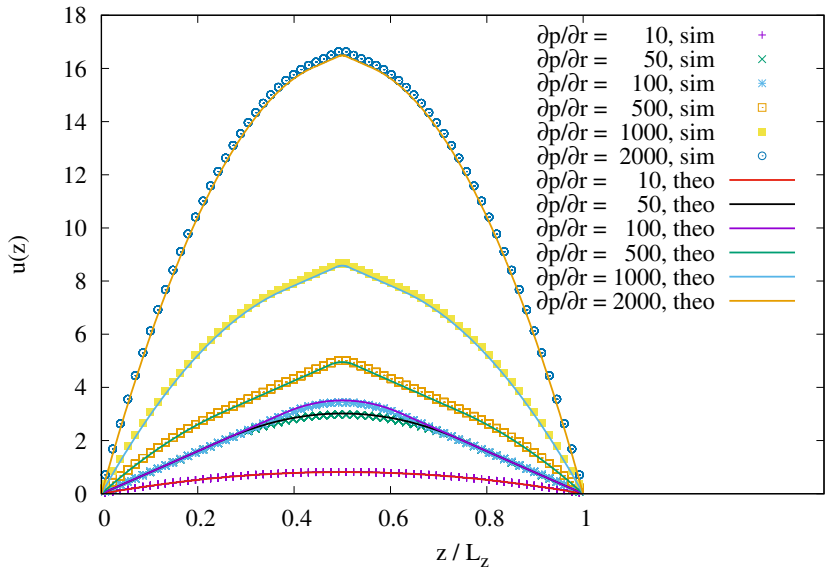

FIG. 8. Comparison of the theory (lines) with the SPH simulations (points) for different pressure gradients. Only steady-state velocity profiles are shown.

In the Fig. 8 the comparison of the analytical steady-state velocity profiles obtained in Sec.II with the numerical SPH results has been depicted for different applied pressure gradients, i.e mapping the three flow regimes discussed above. The agreement is excellent for every $\partial p/\partial r$.

Finally, in Fig. 9 we compare the flow rate Q obtained from SPH simulations with that predicted by the theory. These results serve, both as SPH inverse bi-viscous model validation and as 'a posteriori' confirmation of the analytical results calculated in Sec.II.

IV. CONCLUSIONS

In this work we have presented an analytical derivation of the planar channel flow solution for a DST fluid described by an inverse bi-viscous model and a numerical validation using the Smoothed Particle Hydrodynamic method. The inverse bi-viscous model is characterized by a discontinuous transition in the fluid viscosity at a given critical shear rate $\dot{\gamma}_c$ and offers a possible route to analyze discontinuous shear thickening in suspensions. The model has been regularized by introducing a linear "smooth" transition characterized by a small finite extension $\delta\dot{\gamma}$. In the limit of vanishing $\delta\dot{\gamma}$ the DST behavior is recovered.

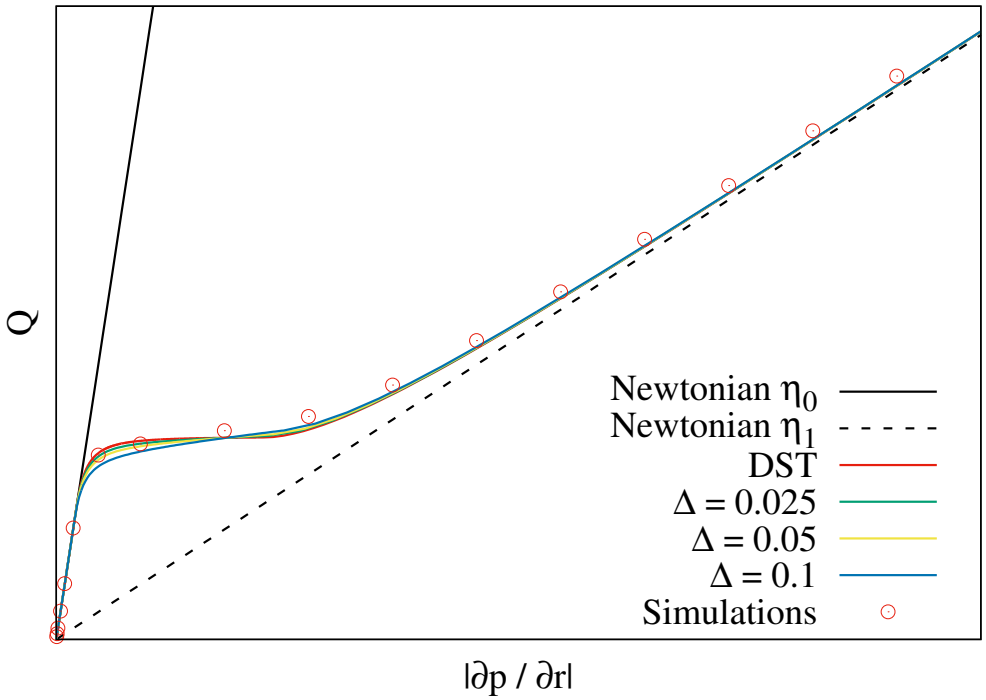

FIG. 9. Flow rate vs pressure gradient. Continuous line: analytical solution. Circles: SPH simulations $\Delta = 0.1$.

Upon sudden application of a constant pressure gradient, the analytical solution for the steady-state velocity profile exhibits non-trivial behavior, i.e. a transition between three flow regimes. (i) At low applied pressure gradients, the classical parabolic profile with low viscosity plateau η_0 is obtained. (ii) At intermediate pressure gradient a two-regions velocity profile is calculated: near-wall layers are characterized by quasi-linear profiles consistent with an almost constant shear rate $\dot{\gamma}_c - \delta\dot{\gamma} < \dot{\gamma} < \dot{\gamma}_c + \delta\dot{\gamma}$, whereas the middle-plane region is parabolic with viscosity η_0. (iii) Finally, at large pressure gradients a three-regions velocity profile is derived. Beside the two-regions located in the middle of the channel, a new near-wall layer with parabolic profiles of viscosity η_1 develops. In the limit of very large pressure gradient, the thickness of this near-wall layer extends towards the center of the channel, eventually pervading the entire space. This corresponds to the limiting parabolic solution of a Newtonian fluid flowing with viscosity η_1.

Despite its apparent simplicity, the inverse bi-viscous model contains more physical information than two simple viscous regimes. In fact, for intermediate pressure gradients a non-linear behavior of the flow rate with enhanced resistance is mathematically required to

exactly match the two viscous regime. This feature allows to capture the essential characteristics of some DST fluids, where return to highly viscous-like behavior is observed after a temporary solid-like response[43].

In terms of practical output, the present work proposes, on one hand, a new analytical solution for simple planar channel flow of a DST fluid, which could be used in the future to develop novel lubrication interaction models between solid particles suspended in a complex DST matrix[35], and it could be performed following the route proposed previously in Ref.[36] for shear-thinning fluids. On the other hand, the present work validates for the first time a SPH model of DST fluid which could be applied in the future to non-homogeneous flow problems, e.g. to enable the simulation of dense DST suspensions within the framework developed in[44,45]. The unique flow rate vs. pressure drop profile provides also valuable guide for engineering devices, such as dampers and self-limiting mechanical elements.

In terms of limitations, the present inverse bi-viscosity formulation captures the essential physics of sudden increase in flow resistance of DST fluids, but modelling is limited to a generalized Newtonian framework. In other words, it neglects the presence of normal stress differences, memory effects as well as complex viscoelasticity of the liquid/solid-like transition which might be relevant in certain applications. Moreover, an homogeneous assumption is made in such a way that DST is uniquely determined by flow-features (i.e. local shear rate) and no effect of the microstructure (e.g. inhomogeneous concentration and/or migration in particle systems) is considered. For a complete historical references on pressure driven flows in suspensions and related migration effects the reader is referred to the seminal work of Nott and Brady[46]. This could be introduced in the model similarly to[47], where an additional scalar field determining the underlying state of the fluid (relaxed/jammed) is considered and coupled to the viscosity. Finally, the current model being characterized by single-value stress/shear-rate relation is unable to predict unsteady solutions and "rheochaos" observed in extremely dense (above 50% solid volume fraction) DST particle suspensions[43]. To remedy this problem a non-linear stress relation could be developed which delivers multiple values of viscosity in a prescribe transitional regime and will be the subject of future research.

V. ACKNOWLEDGEMENTS

Adolfo Vázquez-Quesada and Marco Ellero gratefully acknowledge the financial support provided by the Welsh Government and Higher Education Funding Council for Wales through the Ser Cymru National Research Network in Advanced Engineering and Materials. Computing resources offered by HPC Wales via the project Nr. HPCWT050 (Multiscale particle simulation for complex fluids) is also gratefully acknowledged. Adolfo Vázquez-Quesada also thanks MINECO (Spain) for support under Grant No. FIS2013-47350-C5-1-R is acknowledged.

REFERENCES

[1]N. J. Wagner and J. F. Brady, "Shear thickening in colloidal dispersions," Physics Today **62**, 27–32 (2009).

[2]Y. S. Lee, E. D. Wetzel, and N. J. Wagner, "The ballistic impact characteristics of kevlar woven fabrics impregnated with a colloidal shear thickening fluid," Journal of Materials Science **38**, 2825–2833 (2003).

[3]J. N. Fowler, A. A. Pallanta, C. B. Swanik, and W. N. J., "The use of shear thickening nanocomposites in impact resistant materials," J Biomech Eng. **137**, 32054504 (2015).

[4]H. A. Barnes, "Shear-thickening (dilatancy) in suspensions of nonaggregating solid particles dispersed in newtonian liquids," Journal of Rheology **33**, 329–366 (1989).

[5]R. J. Morgan, "A study of the phenomenon of rheological dilatancy in an aqueous pigment suspension," Transactions of The Society of Rheology **12**, 511–533 (1968).

[6]H. Freundlich and H. L. Roder, "Dilatancy and its relation to thixotropy," Trans. Faraday Soc. **34**, 308–316 (1938).

[7]R. Hoffman, "Discontinuous and dilatant viscosity behavior in concentrated suspensions. ii. theory and experimental tests," Journal of Colloid and Interface Science **46**, 491 – 506 (1974).

[8]J. F. Brady and G. Bossis, "The rheology of concentrated suspensions of spheres in simple shear flow by numerical simulation," Journal of Fluid Mechanics **155**, 105–129 (1985).

[9]D. R. Foss and J. F. Brady, "Structure, diffusion and rheology of brownian suspensions by stokesian dynamics simulation," Journal of Fluid Mechanics **407**, 167–200 (2000).

[10]A. Sierou and J. F. Brady, "Rheology and microstructure in concentrated noncolloidal suspensions," Journal of Rheology **46**, 1031–1056 (2002).

[11]J. Mewis and N. J. Wagner, *Colloidal Suspension Rheology* (Cambridge University Press, 2011) cambridge Books Online.

[12]X. Cheng, J. H. McCoy, J. N. Israelachvili, and I. Cohen, "Imaging the microscopic structure of shear thinning and thickening colloidal suspensions," Science **333**, 1276–1279 (2011).

[13]J. Bender and N. J. Wagner, "Reversible shear thickening in monodisperse and bidisperse colloidal dispersions," Journal of Rheology **40**, 899–916 (1996).

[14]B. J. Maranzano and N. J. Wagner, "Flow-small angle neutron scattering measurements of colloidal dispersion microstructure evolution through the shear thickening transition," The Journal of Chemical Physics **117**, 10291–10302 (2002).

[15]H. M. Laun, R. Bung, S. Hess, W. Loose, O. Hess, K. Hahn, E. Hdicke, R. Hingmann, F. Schmidt, and P. Lindner, "Rheological and small angle neutron scattering investigation of shear-induced particle structures of concentrated polymer dispersions submitted to plane poiseuille and couette flow," Journal of Rheology **36**, 743–787 (1992).

[16]J. W. Bender and N. J. Wagner, "Optical measurement of the contributions of colloidal forces to the rheology of concentrated suspensions," Journal of Colloid and Interface Science **172**, 171 – 184 (1995).

[17]S. Jamali, A. Boromand, N. Wagner, and J. Maia, "Microstructure and rheology of soft to rigid shear-thickening colloidal suspensions," Journal of Rheology **59**, 1377–1395 (2015).

[18]X. Bian, S. Litvinov, M. Ellero, and N. J. Wagner, "Hydrodynamic shear thickening of particulate suspension under confinement," Journal of Non-Newtonian Fluid Mechanics **213**, 39 – 49 (2014).

[19]C. B. Holmes, M. E. Cates, M. Fuchs, and P. Sollich, "Glass transitions and shear thickening suspension rheology," Journal of Rheology **49**, 237–269 (2005).

[20]S. R. Waitukaitis and H. M. Jaeger, "Impact-activated solidification of dense suspensions via dynamic jamming fronts," Nature **487**, 205–209 (2012).

[21]R. Seto, R. Mari, J. F. Morris, and M. M. Denn, "Discontinuous shear thickening of frictional hard-sphere suspensions," Phys. Rev. Lett. **111**, 218301 (2013).

[22]N. Fernandez, R. Mani, D. Rinaldi, D. Kadau, M. Mosquet, H. Lombois-Burger, J. Cayer-Barrioz, H. J. Herrmann, N. D. Spencer, and L. Isa, "Microscopic mechanism for shear

thickening of non-brownian suspensions," Phys. Rev. Lett. **111**, 108301 (2013).

[23]N. Y. C. Lin, B. M. Guy, M. Hermes, C. Ness, J. Sun, W. C. K. Poon, and I. Cohen, "Hydrodynamic and contact contributions to continuous shear thickening in colloidal suspensions," Phys. Rev. Lett. **115**, 228304 (2015).

[24]P. M. Kulkarni and J. F. Morris, "Suspension properties at finite reynolds number from simulated shear flow," Physics of Fluids **20**, 040602 (2008).

[25]F. Picano, W.-P. Breugem, D. Mitra, and L. Brandt, "Shear thickening in non-brownian suspensions: an excluded volume effect," Phys. Rev. Lett. **111**, 098302 (2013).

[26]I. Lashgari, F. Picano, W.-P. Breugem, and L. Brandt, "Laminar, turbulent, and inertial shear-thickening regimes in channel flow of neutrally buoyant particle suspensions," Phys. Rev. Lett. **113**, 254502 (2014).

[27]R. Scirocco, J. Vermant, and J. Mewis, "Shear thickening in filled boger fluids," Journal of Rheology **49**, 551–567 (2005).

[28]S. Guillou and R. Makhloufi, "Effect of a shear-thickening rheological behaviour on the friction coefficient in a plane channel flow: A study by direct numerical simulation," Journal of Non-Newtonian Fluid Mechanics **144**, 73 – 86 (2007).

[29]M. M. Nejad and K. Javaherdeh, "Numerical simulation of power-law fluids flow and heat transfer in a parallel-plate channel with transverse rectangular cavities," Case Studies in Thermal Engineering **3**, 68 – 78 (2014).

[30]L. Ferrs, J. Nbrega, and F. Pinho, "Analytical solutions for newtonian and inelastic non-newtonian flows with wall slip," Journal of Non-Newtonian Fluid Mechanics **175176**, 76 – 88 (2012).

[31]I. Lashgari, J. O. Pralits, F. Giannetti, and L. Brandt, "First instability of the flow of shear-thinning and shear-thickening fluids past a circular cylinder," Journal of Fluid Mechanics **701**, 201–227 (2012).

[32]J. Marn and P. Ternik, "Laminar flow of a shear-thickening fluid in a 90 pipe bend," Fluid Dynamics Research **38**, 295 – 312 (2006).

[33]W. Wu, X. Huang, H. Yuan, F. Xu, and J. Ma, "A modified lattice boltzmann method for herschel-bulkley fluids," Rheologica Acta **56**, 369–376 (2017).

[34]C. D. Cwalina and N. J. Wagner, "Material properties of the shear-thickened state in concentrated near hard-sphere colloidal dispersions," Journal of Rheology **58**, 949–967 (2014).

[35]C. D. Cwalina and N. J. Wagner, "Rheology of non-brownian particles suspended in concentrated colloidal dispersions at low particle reynolds number," Journal of Rheology **60**, 47–59 (2016).

[36]A. Vázquez-Quesada and M. Ellero, "Analytical solution for the lubrication force between two spheres in a bi-viscous fluid," Physics of Fluids **28**, 073101 (2016).

[37]P. Español and M. Revenga, "Smoothed dissipative particle dynamics," Physical Review E **67**, 026705 (2003).

[38]J. J. Monaghan, "Smoothed particle hydrodynamics," Reports on progress in physics **68**, 1703 (2005).

[39]J. P. Morris, P. J. Fox, and Y. Zhu, "Modeling low reynolds number incompressible flows using sph," Journal of computational physics **136**, 214–226 (1997).

[40]M. Ellero and R. Tanner, "Sph simulations of transient viscoelastic flows at low reynolds number," Journal of Non-Newtonian Fluid Mechanics **132**, 61 – 72 (2005).

[41]A. Vázquez-Quesada and M. Ellero, "Sph simulations of a viscoelastic flow around a periodic array of cylinders confined in a channel," Journal of Non-Newtonian Fluid Mechanics **167**, 1–8 (2012).

[42]M. Grilli, A. Vázquez-Quesada, and M. Ellero, "Transition to turbulence and mixing in a viscoelastic fluid flowing inside a channel with a periodic array of cylindrical obstacles," Phys. Rev. Lett. **110**, 174501 (2013).

[43]M. Hermes, B. M. Guy, W. C. K. Poon, G. Poy, M. E. Cates, and M. Wyart, "Unsteady flow and particle migration in dense, non-brownian suspensions," Journal of Rheology **60**, 905–916 (2016).

[44]A. Vázquez-Quesada, R. I. Tanner, and M. Ellero, "Shear thinning of noncolloidal suspensions," Phys. Rev. Lett. **117**, 108001 (2016).

[45]A. Vázquez-Quesada and M. Ellero, "Rheology and microstructure of non-colloidal suspensions under shear studied with smoothed particle hydrodynamics," Journal of Non-Newtonian Fluid Mechanics **233**, 37 – 47 (2016).

[46]P. R. Nott and J. F. Brady, "Pressure-driven flow of suspensions: simulation and theory," Journal of Fluid Mechanics **275**, 157199 (1994).

[47]H. Nakanishi, S.-i. Nagahiro, and N. Mitarai, "Fluid dynamics of dilatant fluids," Phys. Rev. E **85**, 011401 (2012).